Results in Engineering 27 (2025) 105737

Contents lists available at ScienceDirect

Results in Engineering

journal homepage: www.sciencedirect.com/journal/results-in-engineering

Research paper

Compact circular MIMO antenna with defected ground structure (DGS) for improved isolation in 5G sub-6GHz mobile systems

Rania Hamdy Elabd [a,b], Ahmed J.A. Al-Gburi [c,*], Amany A. Megahed [a]

[a] Electronic and Communication Dept., Higher Institute of Engineering and Technology in New Damietta, Damietta 34517, Egypt
[b] Electronic and Communication Dept., Horus University, New Damietta, Egypt
[c] Center for Telecommunication Research & Innovation (CeTRI), Fakulti Teknologi dan Kejuruteraan Elektronik dan Komputer (FTKEK), Universiti Teknikal Malaysia Melaka (UTeM), Durian Tunggal, Melaka 76100, Malaysia

ARTICLE INFO

Keywords:
Circular shaped antenna
Mutual coupling (MC)
MIMO
Defected ground structure (DGS)
Specific absorption rate (SAR)
Wide band
5G Sub 6GHz
Mobile systems

ABSTRACT

This work introduces a compact circular MIMO antenna designed specifically for sub-6 GHz 5 G mobile applications. The antenna features two circular radiating elements arranged orthogonally to each other, incorporating a circular ring and additional side stubs to enhance both bandwidth and impedance matching. A partially slotted ground plane with curved cuts is employed to reduce capacitive effects and further extend the operational bandwidth. The design is implemented on an FR4 substrate with compact dimensions of $0.3\lambda_o \times 0.6\lambda_o \times 0.0242\lambda_o$ at 4.5 GHz, achieving a wide impedance bandwidth of 3.0 to 6.5 GHz—covering major 5 G frequency bands such as n77, n78, and n79. To improve port isolation, a rectangular defected ground structure (DGS) is introduced, effectively reducing mutual coupling down to -53 dB. Both simulated and experimental results show excellent isolation performance (ranging from -15 dB to -55 dB), high radiation efficiency of up to 95 %, and a peak gain reaching 11.5 dBi. Evaluation of MIMO characteristics—including Diversity Gain (DG), Envelope Correlation Coefficient (ECC), and Total Active Reflection Coefficient (TARC)—confirms the antenna's suitability for multiport systems. Additionally, Specific Absorption Rate (SAR) analysis demonstrates compliance with safety standards for handheld device integration. Overall, the proposed antenna offers a robust solution for modern sub-6 GHz 5 G communication systems.

1. Introduction

The fifth-generation (5G) era is approaching rapidly, propelled by continuous advancements in wireless communication technologies [1]. These developments have raised the bar for performance expectations, including ultra-low latency, higher data throughput, and broader bandwidth capabilities. MIMO antenna systems have become an essential component in 5G infrastructure due to their ability to enhance transmission rates, increase channel capacity, reduce latency, and mitigate multipath fading effects [2–4].

However, as per antenna array theory, when antenna elements are placed at distances less than half a wavelength apart, mutual coupling (MC) between elements can significantly degrade system performance. This degradation affects parameters such as beam patterns, radiation efficiency, and impedance bandwidth [5,6]. As such, minimizing MC remains a central challenge in compact MIMO antenna design, particularly in space-limited scenarios.

Over the past few decades, researchers have proposed various decoupling mechanisms to address MC. These techniques can generally be grouped into three main categories based on their operational principles [7]. The first category aims to directly suppress the surface current or electromagnetic wave coupling paths between antenna elements. One widely used solution in this context is the Defected Ground Structure (DGS) [8], which disrupts surface wave propagation by introducing discontinuities in the ground plane, thereby creating a band-stop response and altering the current distribution. However, DGS structures can sometimes result in an elevated Front-to-Back Ratio (FBR), which may affect the radiation performance.

Recent advancements in electromagnetic material design have enabled the development of advanced metastructures with tailored frequency responses. These include Single Negative Metamaterials (SNG) [9], Antenna Decoupling Surfaces (ADS) [10], Frequency Selective Surfaces (FSS) [11], Polarization Conversion Surfaces (PCS) [12], metasurfaces [13], and Electromagnetic Band Gap (EBG) structures [14,

* Corresponding author.
E-mail addresses: ahmedjamal@ieee.org, ahmedjamal@utem.edu.my (A.J.A. Al-Gburi).

https://doi.org/10.1016/j.rineng.2025.105737
Received 18 March 2025; Received in revised form 17 May 2025; Accepted 11 June 2025
Available online 12 June 2025

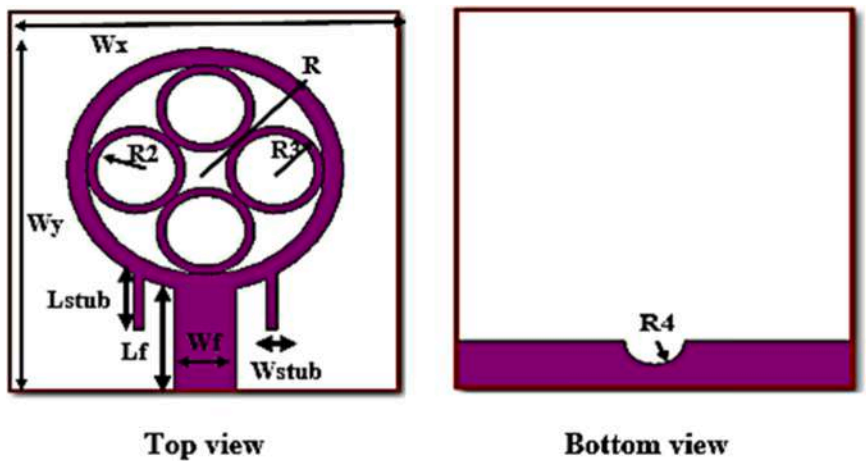

Fig. 1. The structure of planned antenna.

15]. Such engineered surfaces offer promising solutions for mitigating unwanted coupling by suppressing propagating or evanescent modes. For example, metasurfaces placed between MIMO elements have been shown to effectively reduce mutual interaction [11]. This isolation is achieved through spatial band-stop filtering; however, their limited bandwidth and high fabrication costs remain significant challenges.

To overcome some of these challenges, alternative solutions such as out-of-phase reflection structures have been proposed [14], aiming to neutralize coupling fields in dense antenna arrays. However, these methods often require the decoupling surface to be elevated by approximately half a wavelength above the radiating elements, increasing the profile and complexity of the design. A notable example is a metasurface-based isolation wall implemented in a micro base station antenna system with a 1 × 2 configuration [15], where enhanced isolation was achieved using two metasurfaces connected to the ground. Despite its effectiveness, the high cost of metasurfaces compared to traditional copper patches is a concern.

Other decoupling methods rely on incorporating parasitic elements (PE) [16], neutralization lines (NL) [17–19], or decoupling networks (DN) [18] to introduce a new coupling channel that counters the original interaction. For instance, fence-like structures composed of multiple identical slits act as band-stop filters and reduce current coupling between ports [16]. While these slits are effective in improving isolation, they may impact impedance matching at lower frequencies and increase fabrication complexity. Furthermore, NLs and DNs typically involve microstrip circuits or lumped components directly connected to antenna elements, which generate decoupling currents of opposite phase to cancel the original coupling currents. However, these approaches may increase insertion losses and complicate impedance matching [18].

When parasitic elements are placed near but not physically connected to the antenna elements, they can induce counter-phase currents that help suppress coupling. Yet, the induced fields may distort the antenna's radiation characteristics [19]. Many traditional decoupling schemes also demand additional spacing or structural modifications, which add to system size and complexity. Moreover, the insertion loss introduced by decoupling elements can degrade overall system efficiency.

To address these drawbacks, recent research has explored techniques that leverage the antenna's natural characteristics to achieve isolation without external structures [20–23]. These include intrinsic methods like self-decoupling [22], polarization diversity [24], pattern diversity [20], and characteristic mode theory [23]. A key benefit of these techniques is that they maintain compactness and avoid interference with the antenna's radiation behavior. However, these strategies often impose strict constraints on the antenna layout and feed mechanisms. Self-decoupling, while more flexible, lacks a standardized design methodology. An example from [21] uses polarization diversity through parasitic elements to reduce MC, but its effectiveness is limited for broadband antennas. Another novel self-decoupling approach based on near-field manipulation was introduced in [22].

This paper presents a compact circular MIMO antenna specifically designed for sub-6 GHz 5 G mobile applications, incorporating multiple structural enhancements for high performance in limited spaces. A novel single-element design is proposed, featuring a circular ring loaded with four concentric inner loops and extended side stubs, which work together to improve impedance matching and significantly expand operational bandwidth. In addition, a uniquely engineered partial ground plane with curved slits is introduced, which effectively reduces capacitive reactance and contributes to the bandwidth enhancement—a distinctive approach not widely adopted in similar MIMO configurations. The MIMO setup consists of two orthogonally oriented, closely spaced antenna elements (7 mm apart)—a compact layout suitable for modern handheld devices. To achieve high isolation within such a compact footprint, a custom rectangular Defected Ground Structure (DGS) is embedded between the elements, generating decoupling currents that reduce mutual coupling to an impressive −53 dB. This configuration enables exceptional isolation without the need for large metasurfaces or elevated decoupling layers, thus maintaining a low-profile form factor. The proposed system demonstrates a high radiation efficiency (∼95 %) and a peak gain of 11.5 dBi, along with a broad impedance bandwidth from 3.0 to 6.5 GHz, effectively covering all critical sub-6 GHz 5 G bands (n77, n78, and n79). These features make it a promising solution for compact 5 G mobile terminals operating within the sub-6 GHz spectrum.

2. Process and practical investigation

2.1. Layout of the proposed single-element circular shaped antenna

The proposed circular-shaped single-element antenna is exposed in Fig. 1. It was created on a FR4 substrate with a dielectric constant of 4.3 and a loss tangent of 0.025 using a CST simulator. The substrate's thickness is 1.6 mm. The circular antenna's construction involves of a main circular ring with four smaller circular rings inside of it that are linked to each other, as well as stubs on each side of the main ring to rise the antenna's bandwidth. The antenna's bandwidth is increased and capacitive reactance is further lessened by employing partial ground with curved slits. The printed circular antenna that is partly grounded has dimensions of 20 × 22 mm^2.

The guided process for constructing an antenna patch is represented in Fig. 2(a). To mathematically analyze the geometry (Eqs. (1–7) [25]) of the antenna shown in Fig. 1, and relate its dimensions to the resonant

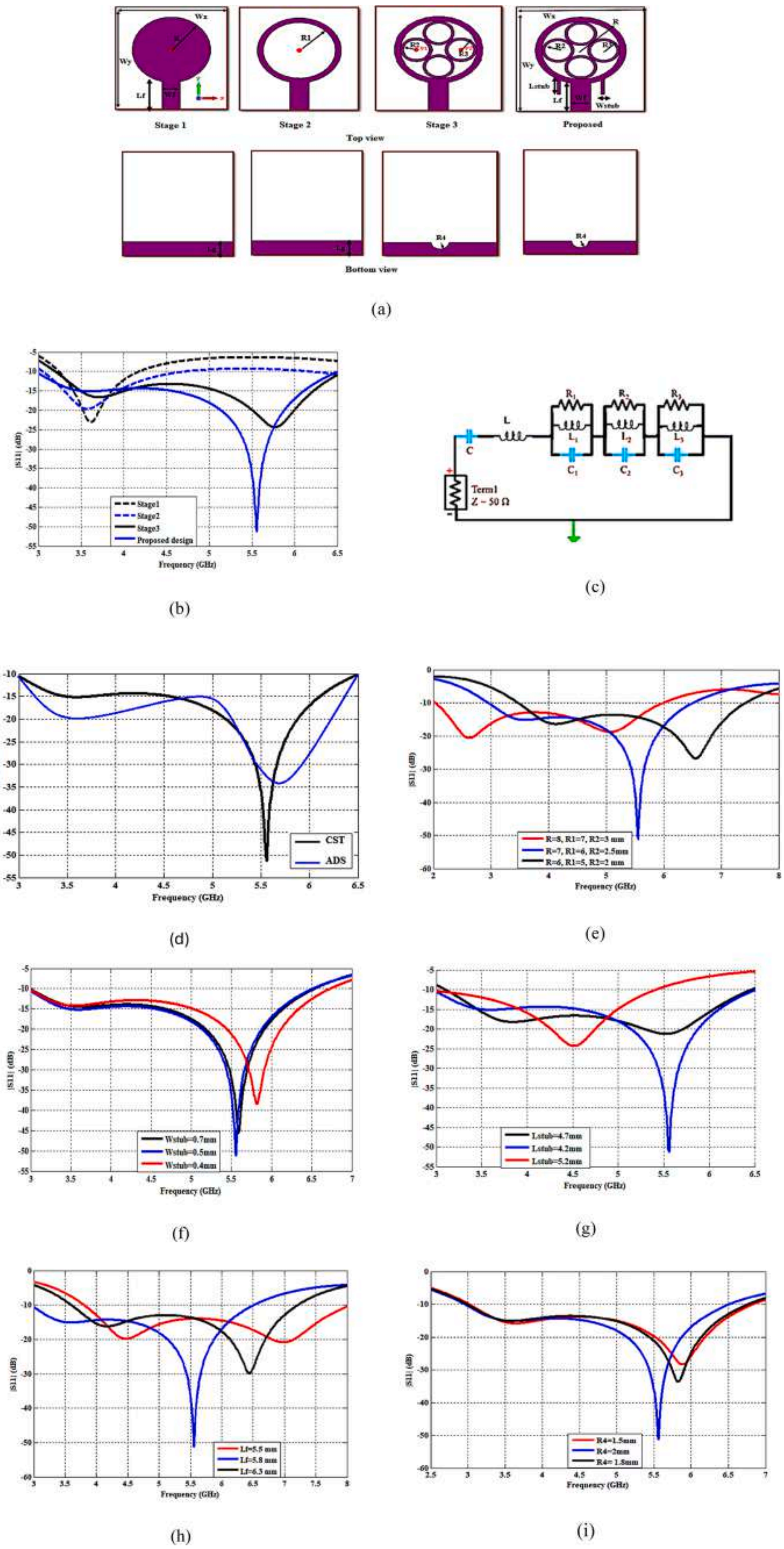

Fig. 2. (a) Phases of the planned circular shaped antenna's progressive design. (b) S11 (dB), (c) EC of the proposed wide band antenna, (d) evaluations of ADS and CST and (e), (f),(g), (h), (i) parametric analysis of S11 at different dimensions (R, R1, R2, R4, Lstub, Wstub, Lf).

Table 1
Enhanced parameters of the suggested circular shaped antenna (millimeters).

Wx	Wy	Wf	Lf	Wstub	Lstub	Lg	R	R1	R2	R3	R4
20	22	3.18	5.8	0.5	4.02	3.2	7	6	2	2.5	2

Table 2
The circuit's electrical parts values correspond to each other.

C	L	R1	L1	C1	R2
1.53 pF	3.94 nH	35 Ω	2.523 nH	3.92 pF	2.32 Ω
L2	C2	R3	L3	C3	L2
2.35 nH	2.98 pF	80.9 Ω	1.31 nH	0.598 pF	2.35 nH

frequency, we need to treat the circular ring and stub-loaded structure as a planar antenna with multiple resonant paths. The antenna features: a circular ring (outer radius R) with inner circular stubs (R_1, R_2, R_3), feed line with length L_f and width W_f, a rectangular stub of length L_{stub}, and slot in the ground with radiusR_4

The dominant resonance of a circular ring-shaped monopole can be approximated using the effective circumference:

$$C_{eff} \approx 2\pi R_{avg}, \text{ where } R_{avg} = \frac{R + R_1}{2} \tag{1}$$

And the corresponding resonant frequency is:

$$f_{res} \approx \frac{C}{C_{eff}\sqrt{\varepsilon_{eff}}} = \frac{C}{2\pi R_{avg}\sqrt{\varepsilon_{eff}}} \tag{2}$$

Where: c is the speed of light in free space, and ε_{eff} is the effective dielectric constant (depends on substrate permittivity and structure)

For a microstrip structure:

$$\varepsilon_{eff} = \frac{\varepsilon_r + 1}{2} + \frac{\varepsilon_r - 1}{2}\left(1 + 12\frac{h}{W_f}\right)^{-0.5} \tag{3}$$

Where: ε_r is the substrate relative permittivity (4.4 for FR4), h is the substrate height, and W_f is the feedline width.

The stub and feedline affect impedance matching and can support additional resonances: a quarter-wave stub introduces resonance when its length satisfies:

$$L_{stub} \approx \frac{\lambda_g}{4} = \frac{C}{4f\sqrt{\varepsilon_{eff}}} \tag{4}$$

Similarly, the feedline should be matched and typically approximated by:

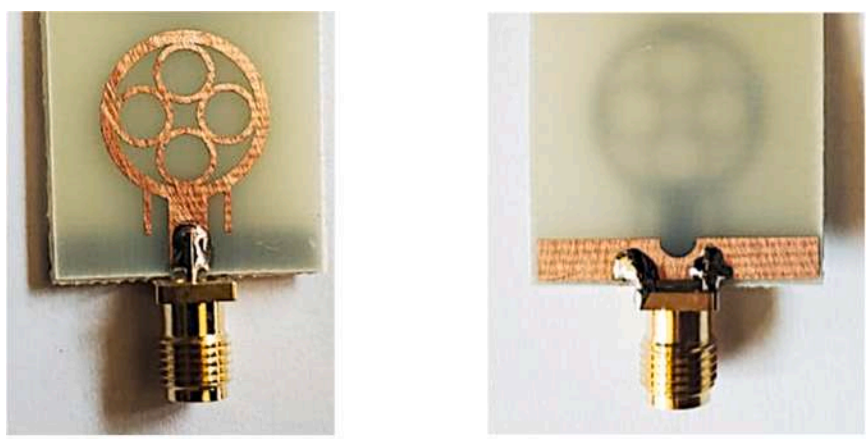

(a) (b)

Fig. 3. The constructed prototype of the envisioned antenna is illustrated alongside the relevant measurements: (a) frontal perspective, and (b) rear perspective.

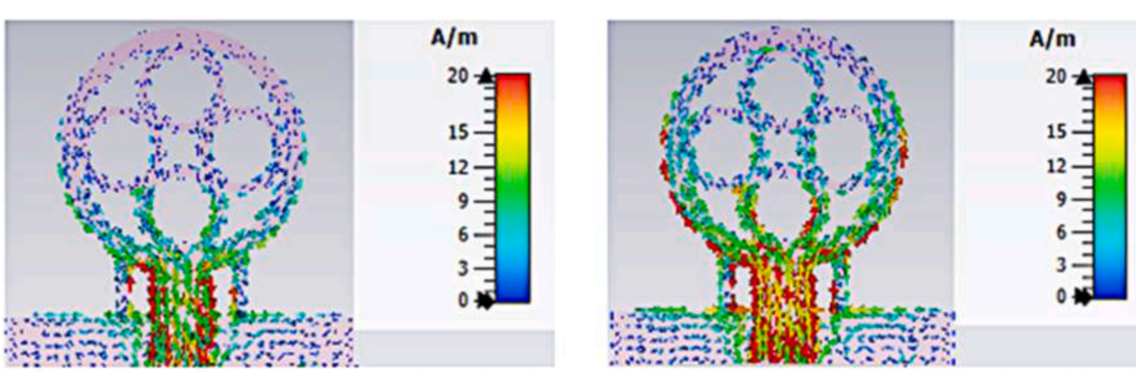

3.3 GHz 4.5 GHz

Fig. 4. Surface current spreading on the antenna's radiating patch.

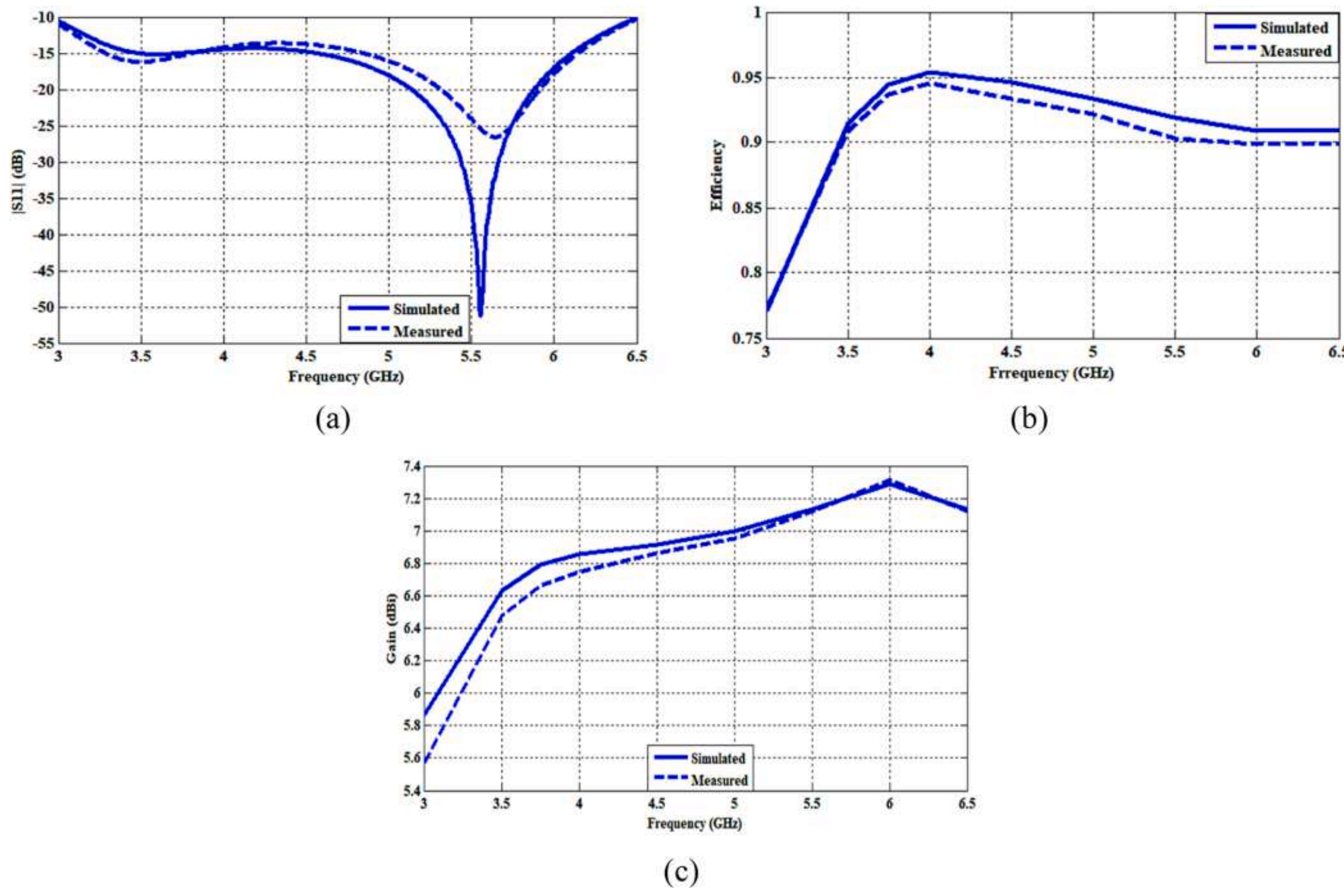

Fig. 5. The measured and simulated parameters of circular shaped antenna. (a) S11 (dB), (b) Efficiency, and (c) Gain.

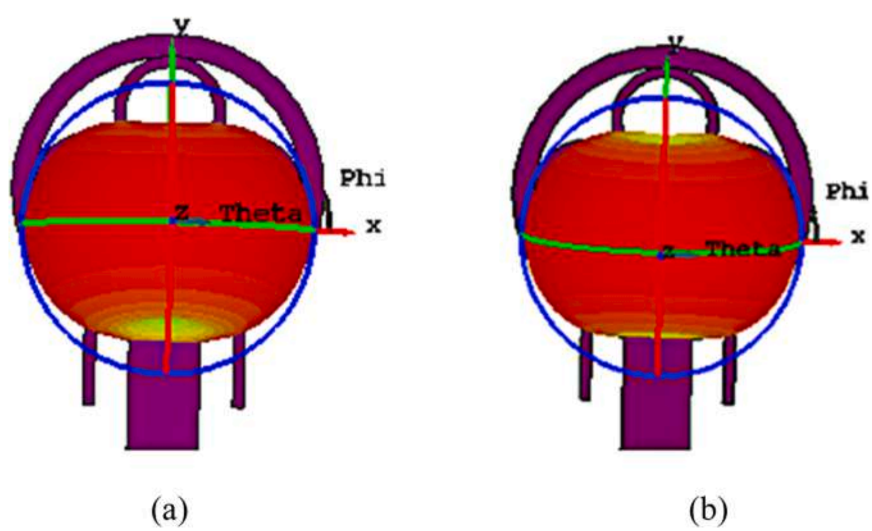

Fig. 6. Single-element antenna's three-dimensional beam at frequency (a) 3.3 GHz, and (b) 4.5 GHz.

$$L_f \approx \frac{\lambda_g}{4}, \text{ depending on the matching section} \tag{5}$$

The slot in the ground (radius R_4) behaves like a defected ground structure, introducing a notch or band-reject behavior at certain frequencies. The resonance due to the circular slot can be estimated by:

$$f_{DGS} \approx \frac{C}{2\pi R_4 \sqrt{\varepsilon_{eff}}} \tag{6}$$

Since the antenna includes multiple circular elements and stubs, the overall resonance is:

$$f_n \approx \frac{C}{2\pi R_n \sqrt{\varepsilon_{eff}}}, \quad R_n \in R, R_1, R_2, R_3, R_4 \tag{7}$$

Each ring or slot supports one or more modes, leading to multi-band behavior.

Table 1 lists the geometric properties of the circular-shaped antenna. The first step design is seen to function in the restricted variety between

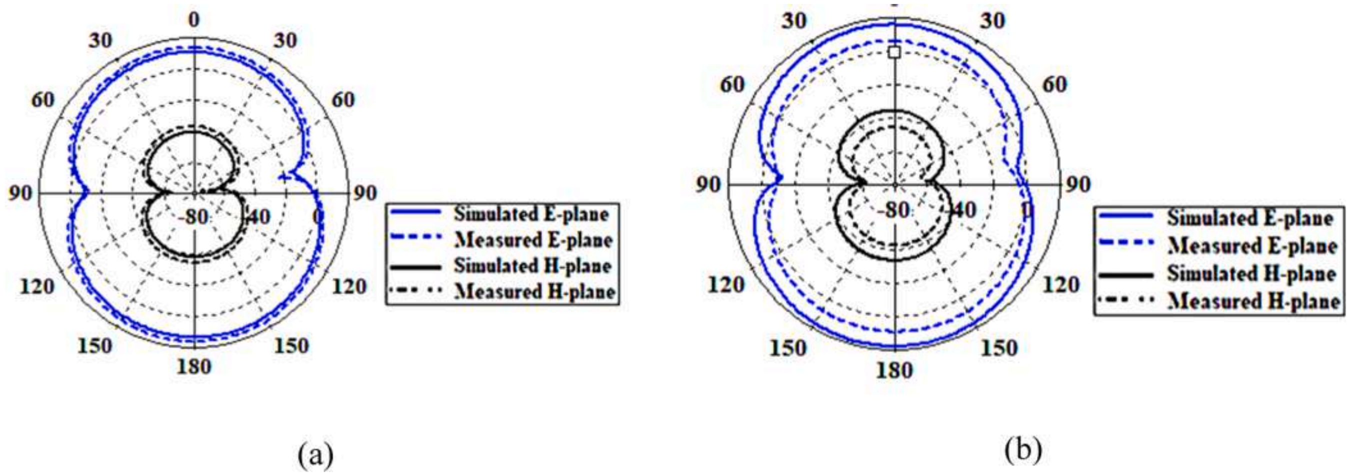

Fig. 7. Patterns of radiation for the suggested antenna at (a) 3.3 GHz, and (b) 4.5 GHz.

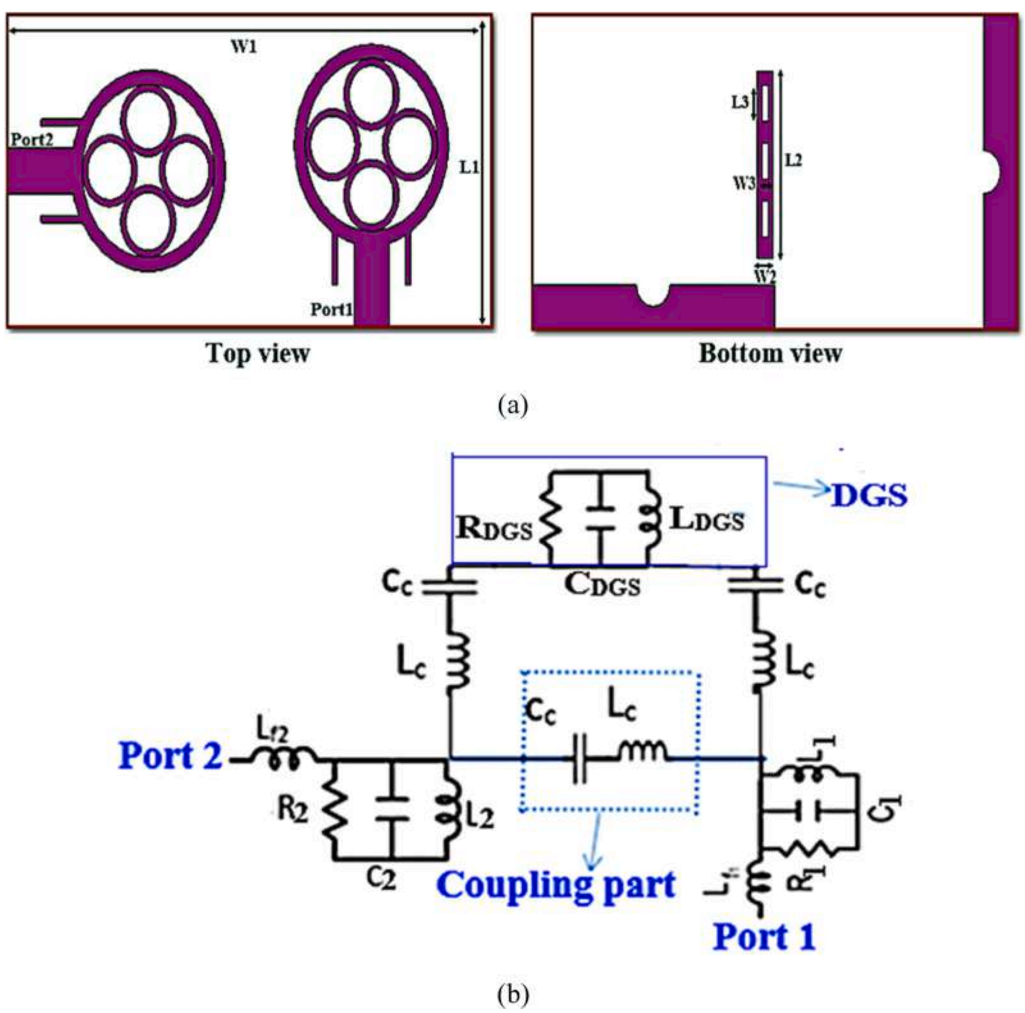

Fig. 8. (a) The MIMO array's geometry and (b) equivalent circuit of MIMO.

3.25 GHz and 4.19 GHz. In the second phase, as can be seen, a circular disk with radius R1 is removed from the main disk to make the main Ring, which improves impedance matching and produces a broad band from 3.05 GHz to 4.52 GHz. In the third step, as shown in Fig. 2(a), curving slits are formed in the middle of the partial ground and four rings are inserted inside the ring patch linked to each other. As displayed in Fig. 2(b), the adding of four rings often results in UWB response from 3.25 GHz to 6.5 GHz and enhances impedance matching. Further impedance matching is accomplished by cutting a curved slit in the partial ground plane and adding a stub on both side of the main ring, as demonstrated in the recommended circular shaped antenna. The inclusion of stubs frequently produces UWB reaction between 3 GHz and 6.5

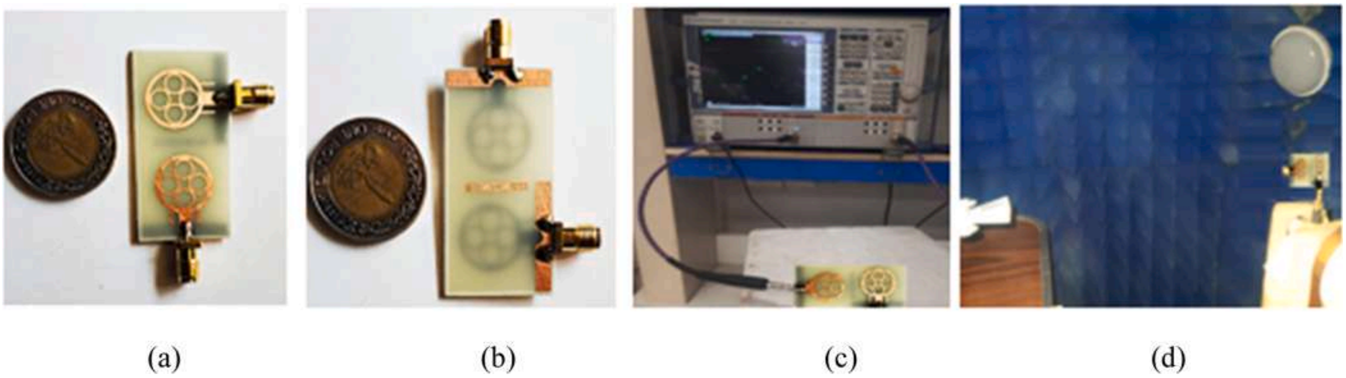

Fig. 9. MIMO antenna array fabrication: (a) frontal perspective, (b) rear perspective, and (c), (d) measurement setup.

Table 3
Optimized parameters of the planned MIMO a array (millimeters).

W1	W2	W3	L1	L2	L3
44	1.5	0.5	22	13	2.5

GHz. In Fig. 2(c), the equivalent circuit is displayed. The design and simulation procedures are done with using CST Microwave Studio 2019.

Fig. 2 presents the parametric analysis of the proposed wideband circular shaped antenna, primarily focusing on the S11 (dB) characteristic. Fig. 2a illustrates the evolution of the S11 response as the radii R, R1, and R2 are systematically adjusted while keeping R4 constant. This reveals a clear sensitivity of the resonant frequency and bandwidth to these inner circular dimensions, suggesting a crucial role in defining the antenna's initial operating band. Figs. 2e through 2i delve into the impact of stub dimensions, specifically Wstub and Lstub, and the feed line length Lf. Variations in Wstub (see Fig. 2f) demonstrate a noticeable influence on the impedance matching level across the operational frequency range, indicating its importance in achieving optimal power transfer. Similarly, altering LStub (see Fig. 2 g) appears to fine-tune the upper frequency band and the depth of the impedance matching. The feed line length Lf (Fig. 2h) exhibits a significant effect on both the resonant frequencies and the overall bandwidth, highlighting its critical role in impedance transformation and broadband performance. Finally, Fig. 2i explores the impact of the outer radius R4, showcasing its influence on the lower frequency band and the impedance matching characteristics. Collectively, this parametric study provides valuable insights into the intricate relationship between the antenna's physical dimensions and its reflection coefficient, offering a pathway for precise

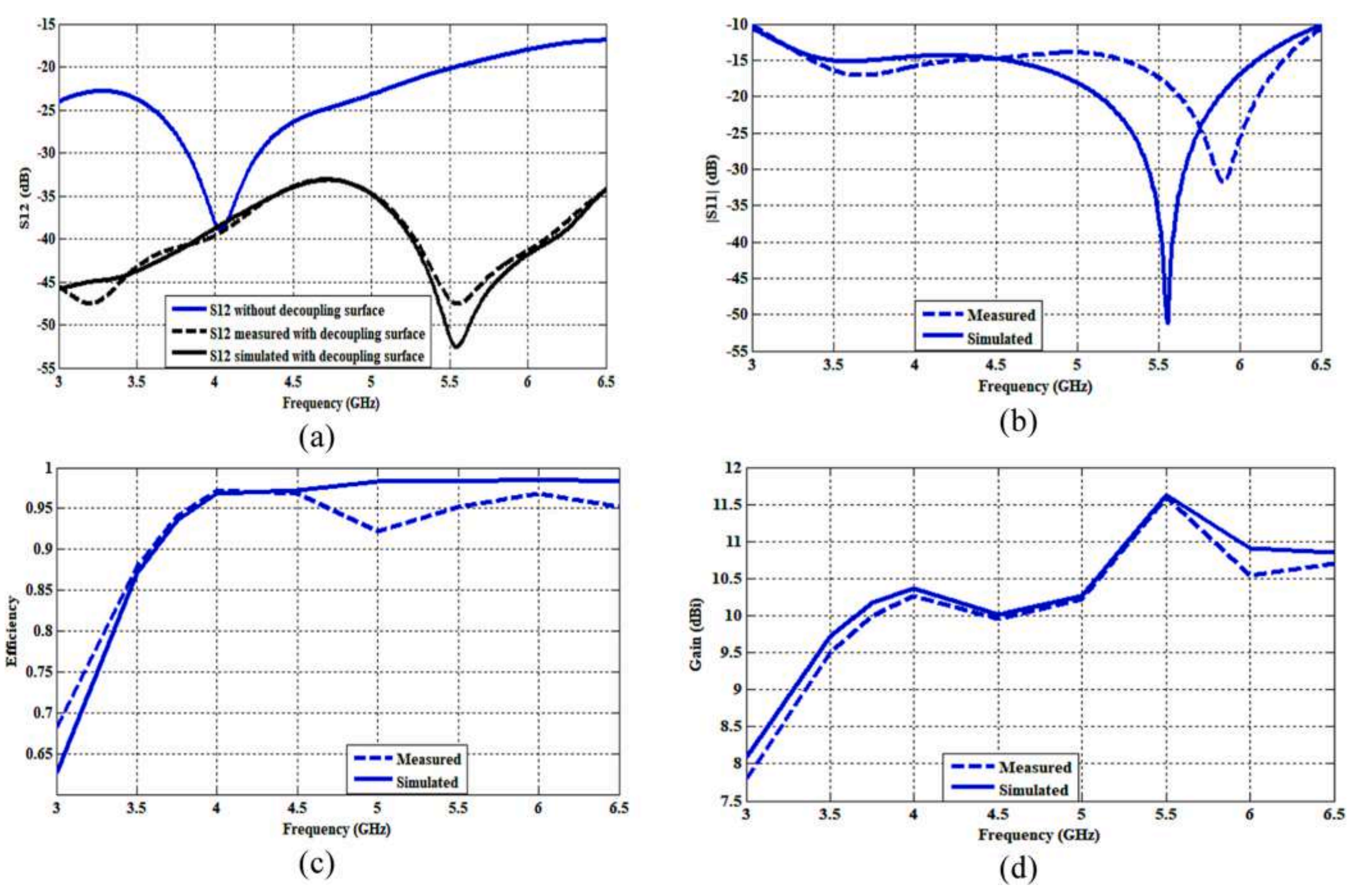

Fig. 10. Characteristics of the suggested MIMO antenna: (a) Isolation, (b) Reflection coefficient, (c) Efficiency, and (d) Gain.

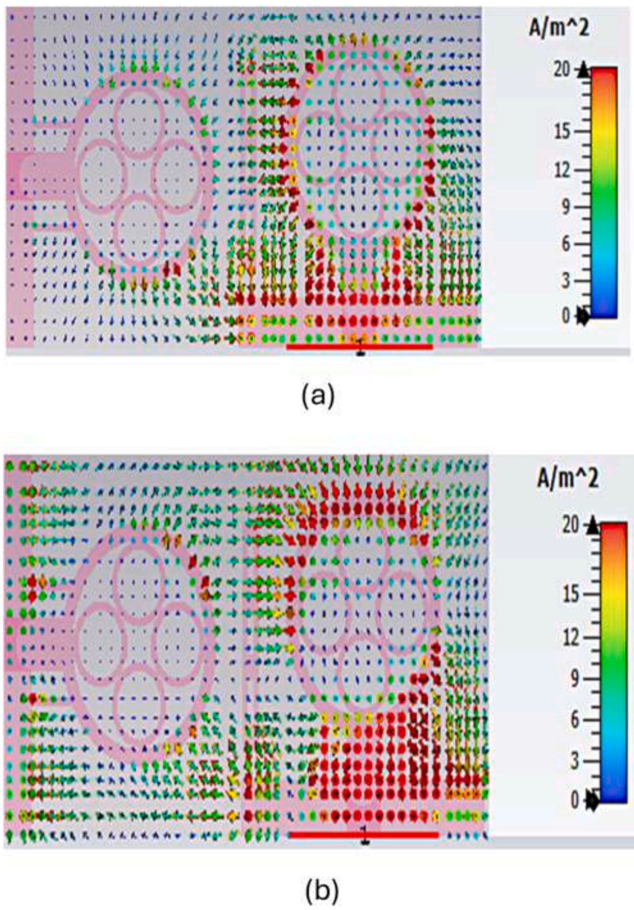

Fig. 11. Surface current patterns on the proposed MIMO antenna at frequencies (a) 3.3 GHz and (b) 4.5 GHz.

tailoring of the antenna's wideband performance through careful selection and optimization of these key parameters.

2.2. Equivalent circuit (EC) diagram

To understand the wideband features of the wide band antenna, a comparable circuit architecture was created in the advanced design system (ADS) program, as shown in Fig. 2(c).

This circuit is constructed on the degeneration Foster canonical (DFC) system, which is broadly used for characterizing wide band antennas. An antenna with broadband features may be thought of as a radiating device that creates several closely spaced resonances, some of which cross over to form adjacent bands. The simulation results for the comparable circuit and the perfect simulation are contrasted, as shown in Fig. 2(d). An examination of each resonance band is possible thanks to the parallel connections between RLC lumped parts. To achieve a wideband characteristic, a number of parallel-associated RLC circuits with closely spaced bands can be linked in series. The capacitance and inductance, symbolized by the letters C and L, respectively, are displayed in Fig. 2(c) while the wideband antenna is resonating at the essential lower style.

The three parallel RLC circuits connected in series enable the lasting higher resonances. The resistors R1, R2, and R3 indicate the radiation resistances of the interrelated resonances. The left RLC circuit, made up of R1, C1, and L1, regulates the impedance matching within the operational band. The center RLC tank, made up of R2, C2, and L2, regulates the lower side of the wideband. R3, C3, and L3 make up the right RLC circuit, which regulates the higher frequencies. The values of the electrical components utilized in the similar circuit are shown in Table 2.

2.3. Simulation and testing setups

The built-in circular antenna, intended to function in the 3 to 6.5 GHz frequency range, is drawn in Fig. 3. This band of frequencies includes 5 G sub-6 GHz. The photolithographic modeling of the proposed antenna using the commercial CST 2019 program is shown in Fig. 3, which sheds light on the fabrication process. The antenna is constructed on a 1.6 mm thick FR4 material substrate with a dielectric constant ε_r of 4.3 and a loss tangent of 0.025. The matching surface currents at 3.3 GHz and 4.5 GHz are drawn in Fig. 4 to help visualize the current distribution on the antenna's surface. As shown in Fig. 4, the transmission feed line and the circular radiating patch show the major current receipt. The possibility of expanding the bandwidth is shown by the concentration of currents nearer the circular antenna's surface.

The reflection coefficients indicate an evaluation of the observed and simulated values, as exposed in Fig. 5(a). The S11 findings illustrate that the antenna can operate across the specified bandwidth, which is 3 to 6.5 GHz, with reflection coefficients as low as −10 dB. The single element of the suggested antenna is driven via a 50-ohm microstrip feed. Additional variations in efficiency and gain are presented in Figs. 5(b) and (c), where the efficiency around 95 % while the gain changes range from 5.8 to 7.3 dBi, respectively. Figs. 6 and 7 show the 3D and 2D shapes features at frequencies of 3.3 GHz and 4.5 GHz, respectively. Fig. 7 displays the two-dimensional (2D) radiation shapes for the planes E and H. The 3.3 GHz and 4.5 GHz frequency bands' radiation characteristics were computed. As seen in Fig. 7, the antenna has bidirectional characteristics for the E-plane and omnidirectional capabilities for the H-plane. Additionally, across the operating spectrum, the provided antenna exhibits good coverage and nearly continuous response.

3. Development and structure of a dual-port MIMO antenna

This section describes how to set up a dual-port circular MIMO antenna and the method for enhancing component isolation. We outline the DGS reduction strategy to achieve superior port isolation. As seen in Fig. 8a, the DGS architecture is rectangular in shape and uses three slots in the middle of the ground plane. The planned MIMO array design scopes are 22 mm × 44 mm × 1.6 mm. Figs. 8 show the arrangement of two identical single circular antenna devices. Each unit is spaced 7 mm apart and is oriented orthogonally to the other units. The FR4 substrate, which has 4.3 value of dielectric constant, aids as the basis for the planned antenna array. The equivalent circuit consists of inductance (L), resistance (R, which is set to 50Ω for impedance matching), and capacitance (C). The components C and L are responsible for electric and magnetic coupling between the antenna elements, respectively. Due to the close spacing between the antennas, mutual coupling becomes a significant issue. To mitigate this effect, a DGS (R_{DGS}, L_{DGS}, C_{DGS}) is introduced between the antennas as shown in Fig. 8b This element adds additional capacitance, enhancing isolation between the antenna elements. As a result, it enables the generation of a decoupling current that effectively reduces mutual coupling and improves overall isolation performance.

Fig. 9 shows the measuring apparatus and the fabricated MIMO antenna array. The suggested MIMO dimensions with DGS are displayed on Table 3. An antenna array simulation is carried out using CST Microwave Studio 2019. Every element receives independent stimulation by a distinct 50 Ω terminal. It's vital to keep in mind that nearby antennas are always somewhat linked. The MC in a two-port array is shown in Fig. 10 (a), both with and without the use of isolation tools. As you can see, in the event that DGS is not present, there is insufficient isolation in the relevant frequency band. Fig. 10(a) illustrates that, in contrast, the isolation while inserting DGS is as high as −53 dB.

4. Findings and discussion

The antenna array covers the frequency range of 3 to 6.5 GHz, as

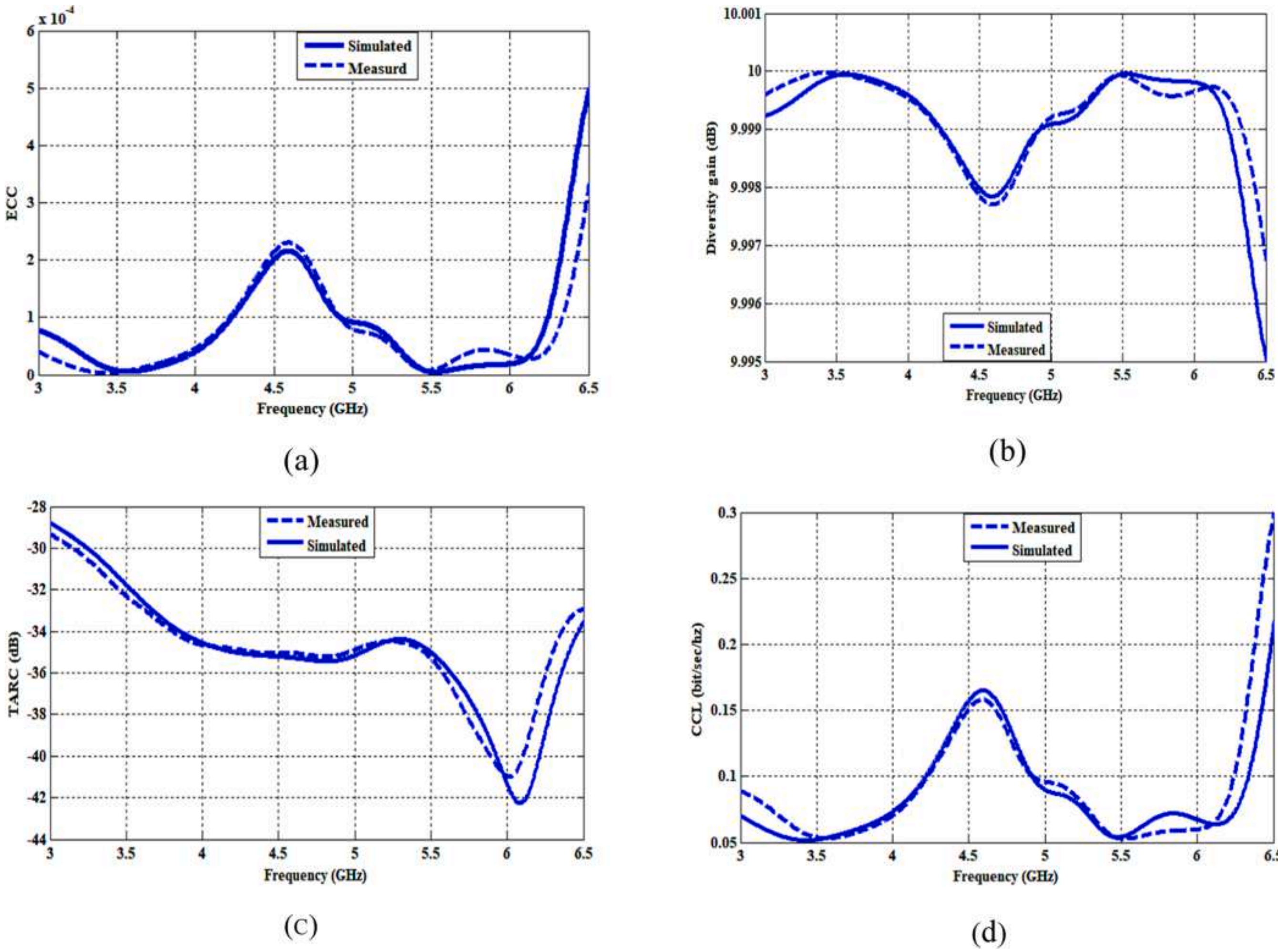

Fig. 12. MIMO antenna features, including (a) ECC, (b) DG, (c) TARC, and (d) CCL.

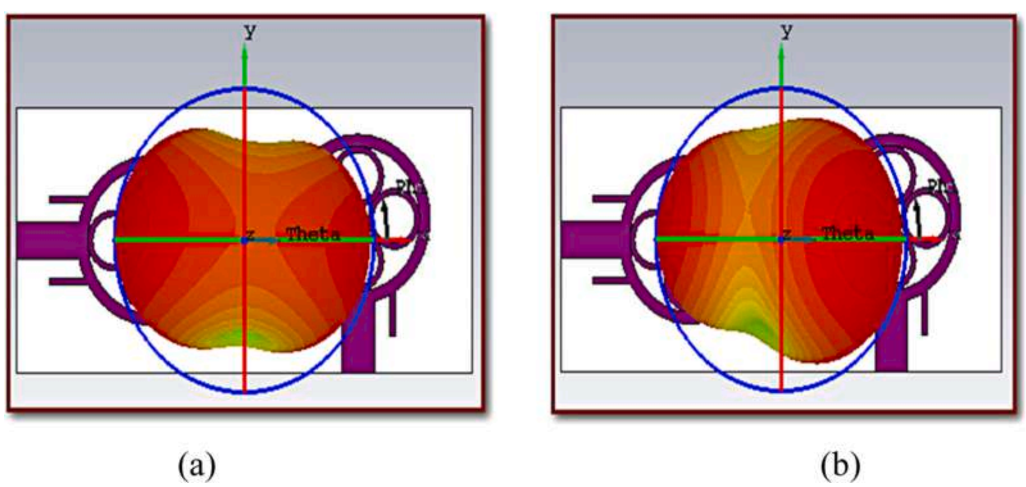

Fig. 13. 3D radiation of single element antenna design at frequency (a) 3.3 GHz, and (b) 4.5 GHz.

presented in Fig. 10(b). The link between measurement and simulation is altered by the connection. Figs. 10(c) and (d) show that the efficiency fluctuates roughly 95 % and that the highest gain is about 11.5 dBi.

Fig. 11 demonstrates the surface current distributions, which provide additional evidence of the impression of the DGS on antenna performance. The current is largely concentrated at the DGS, which results in high inductive impedance. The fall in MC is due to the other antenna components producing essentially no current.

4.1. MIMO parameters

The MIMO antenna's reliability is weighed based on multiple parameters. The Effective Channel Capacity is a crucial dynamic metric that is utilized to evaluate its efficacy (ECC). One important

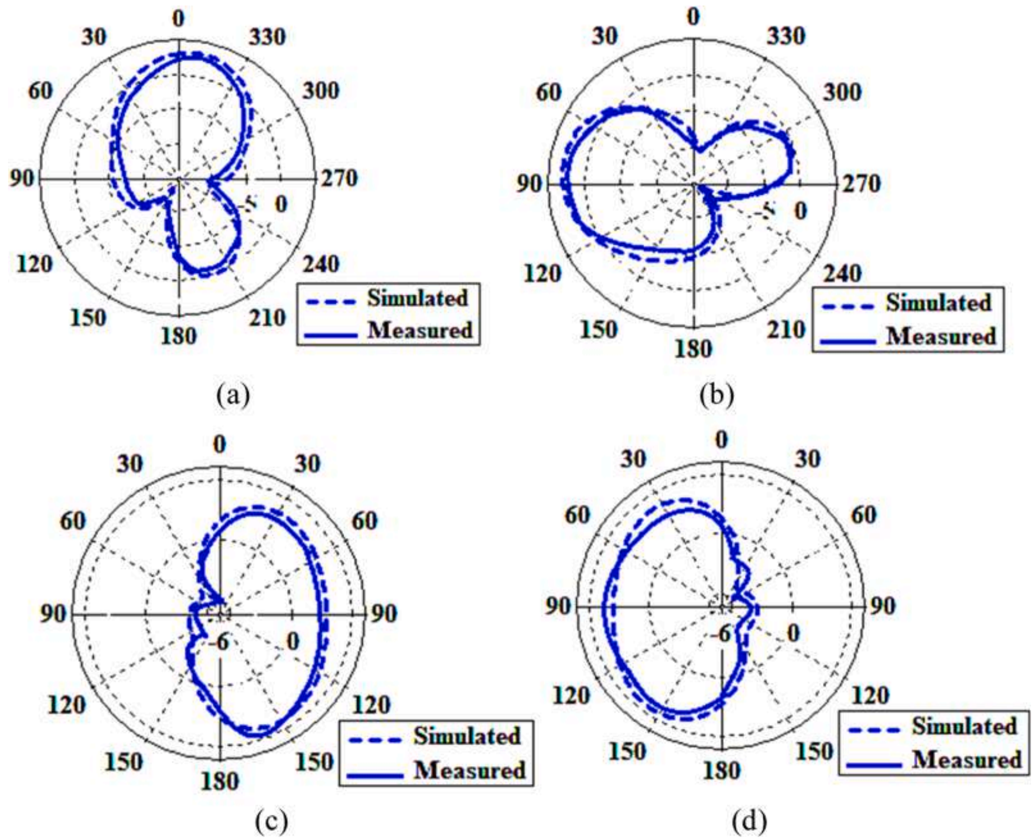

Fig. 14. The 3.3 GHz radiation patterns with θ adjusted to 90 degrees are shown. The patterns for ports 1 and 2 are displayed in subfigures (a) and (b), individually. Subfigures (c) and (d) display the beam forms for ports 1 and 2, respectively, for φ equal to 0 degrees at the same frequency.

performance statistic for the MIMO is ECC, this can be computed from the S-parameters with Eq. (8).

$$\rho_{mn} = \frac{\left| \int \int_0^{4\pi} \left[\vec{F_m} \ (\theta, \Phi) \times \vec{F_n} \ (\theta, \Phi) \right] d\Omega \right|^2}{\int \int_0^{4\pi} \left| \vec{F_m} \ (\theta, \Phi) \right|^2 d\Omega \int \int_0^{4\pi} \left| \vec{F_n} \ (\theta, \Phi) \right|^2 d\Omega} \tag{8}$$

Where ρ:ECC, $F(\theta, \Phi)$: the antenna beam patterns, *m or n* are the number of the antenna.

The results of ECC employing DGS Structure between elements are roughly less than 6×10^{-4}, as exposed in Fig. 12(a). The transmission power loss that occurs on the MIMO structure as soon as the diversity strategy is applied is called DG. The following Eq. (9) is used to determine this parameter:

$$DG = 10\sqrt{1 - (ECC)^2} \tag{9}$$

Third element following the connection between ports is TARC, a measure used for evaluating a MIMO antenna's efficacy. Fig. 12(b) demonstrates the diversity gain (DG), it is nearly 9.9979. The proportion of the square root of the entire incident power to the square root of the total reflected power is acknowledged as TARC. It may be assessed using the following formula, which is given in reference [26]:

$$\Gamma = \sqrt{\frac{\left|s_{ii} + s_{ij}e^{j\theta}\right|^2 + \left|s_{ji} + s_{jj}e^{j\theta}\right|^2}{2}} \tag{10}$$

In this instance, θ represents the input phase angle, fluctuating from 0^o to 180^o, with a step raise of 30^o.

The input phase angle in this case is represented by θ, which has a step increment of 30^o and ranges from 0^o to 180^o. Ports 1 and 2 have reflection coefficients of s_{ii} and s_{jj} individually.

Fig. 12(c) displays the TARC for the recommended design that makes use of the DGS approach. The TARC of the array is ≤ -28 dB. CCL has to be <0.4 bits/s/Hz in order to be wanted. Since it is ≤ 0.3 bit/s/Hz, all three scenarios satisfy CCL. Results for the CCL are displayed in Fig. 12 (d).

Figs. 13 and 14 show the 3D and 2D shapes features at frequencies of 3.3 GHz and 4.5 GHz, correspondingly. The suggested MIMO system's 3.3 GHz radiation patterns, as shown by modeling and experiment, are shown in Fig. 14. The primary lobes in Figs. 14(a) and 14(b) are clearly oriented toward theta = 90 degrees and perpendicular to one another. Furthermore, there is a 90-degree phase variance in the E-plane patterns. On the other hand, as Figs. 14(c) and (d) show, the H-plane forms show a 180-degree phase shift between antennas #1 and #2. All antennas, however, have the identical E-plane designs.

4.2. Radiation properties and the effect of user proximity (hand and head) on radiation behavior

When using a mobile phone, the amount of electromagnetic radiation (EM) that can be absorbed by the human body is measured using a metric called SAR [1,2]. Given that the planned antenna array is mounted on the rear cover, it is needed to estimate the SAR value. A dielectric substance with a permittivity of 3.32 and a loss tangent of 0.002 is used to make the rear cover. Fig. 15(a) shows the antenna design with the rear cover, which has extents of $150 \times 70 \times 1.2$ mm^3. The proposed antenna is projected to be used with mobile phones, so it is necessary to estimate its SAR. The arrangement architecture uses a human head phantom model to evaluate the amount of electromagnetic radiation that the human head absorbs, as Fig. 15(b) shows. The antenna is placed at a 65°-degree angle with respect to the negative vertical axis. The SAR value is affected by the separation distance between the antennas and different body components, as reference [27,28] discusses. Our work's simulation positions the antenna array 5 mm away from the

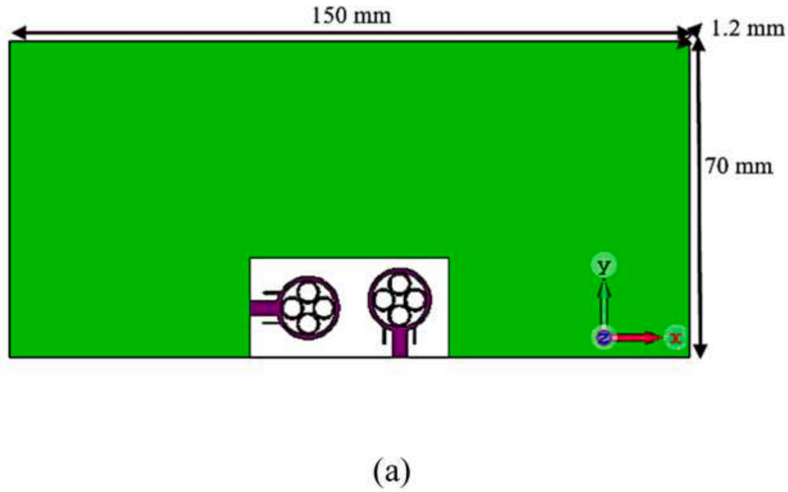

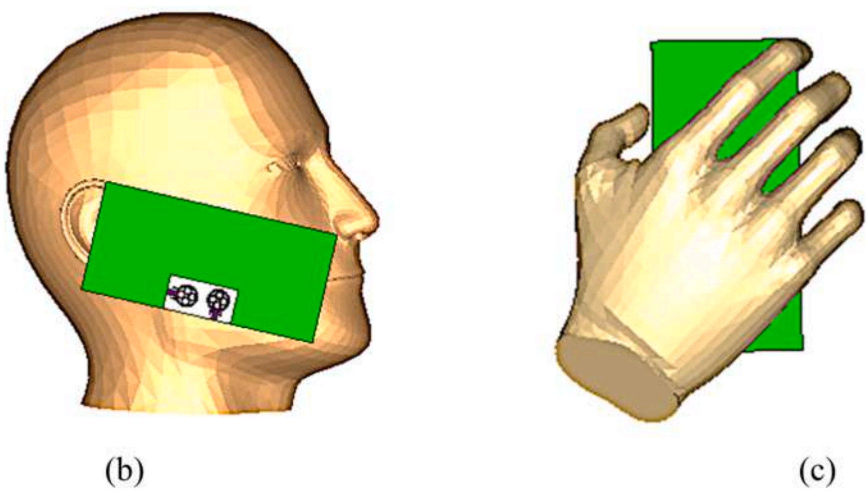

Fig. 15. (a) Schematic of MIMO antenna with dielectric back cover; (b) antenna arrangement configuration using hand phantom prototypical; and (c) antenna proposal for SAR investigation using head phantom prototypical.

head phantom prototypical, or more precisely, close to the mouth and ear areas. The configuration of MIMO is shown over a Single Hand Mode prototypical (SHM) in Fig. 15(c), which is intended to assess the antenna's performance in data mode. The antenna is oriented and placed in a way that maximizes user comfort in various settings. Specifically, there is a little distance of around 0.2 mm between the MIMO antenna's ground plane and the hand phantom model. To assess the antenna's data mode act, Fig. 15(c) shows the antenna configuration over a Single Hand SHM. In order to optimize user comfort in a range of conditions, the antenna is slanted. especially because there is a little gap—roughly 0.2 mm—between the antenna's surface and the hand phantom modeling.

Fig. 16 shows the SAR value that was simulated. Notably, the considered SAR is within the permissible variety of conventional SAR values (1.6 W/Kg). Regarding sub-6 GHz 5 G, the effect of the man's hand on the antenna array is evaluated at resonance frequencies of 3.3 GHz and 4.5 GHz. Most outstandingly, positioning the antenna above the hand has a big impact on how effective it is. As shown in Table 3, the simulated SAR1g and SAR10g results for the proposed structure operating at 4.5 GHz with 15 dBm power input are provided. The findings indicate full compliance with the FCC and ICNIRP regulatory limits. Specifically, the SAR10g values at frequencies of 3.3 GHz and 4.5 GHz are 0.0236 W/kg and 0.342 W/kg, respectively, both well within the acceptable thresholds. Fig. 17 shows how the S-parameters have changed. It is discovered that the impedance matching decreases when the SHM introduces dielectric loading. The SAR1g and SAR10g simulations of the suggested structure at 5 and 10 mm distances are displayed in Table 4.

5. Comparison with related works

Despite the production of wideband, circular-shaped MIMO antennas with superior isolation, low profile and increased gain among other design constraints make it exciting to sacrifice compressed dimensions. The little size, quantity of ports, frequency range, isolation methods, increased isolation levels, gain, efficiency, ECC, and DG of the mentioned MIMO array are all exceptional. It performs better than models #1 through #11 in comparison. The MIMO system analysis situs that was provided are compared and their individual competitive advantages are highlighted in Table 5. To simplify the assessment of Specific Absorption Rate (SAR) data, Tables 5 have been provided.

6. Conclusion

In this research paper, we presented a dual-port circular MIMO system with strong port isolation. The effectiveness of the DGS technique in reducing mutual coupling (MC) between antennas was carefully evaluated. Simulations were conducted using CST to optimize the radiating element sizes. The proposed MIMO antenna demonstrated excellent isolation of −53 dB across the entire spectrum. The DGS approach enhanced isolation by introducing additional capacitance into the circuit. As a result, the antenna achieved a peak gain of 11.5 dBi, 95 % efficiency, and strong diversity performance. Key MIMO metrics,

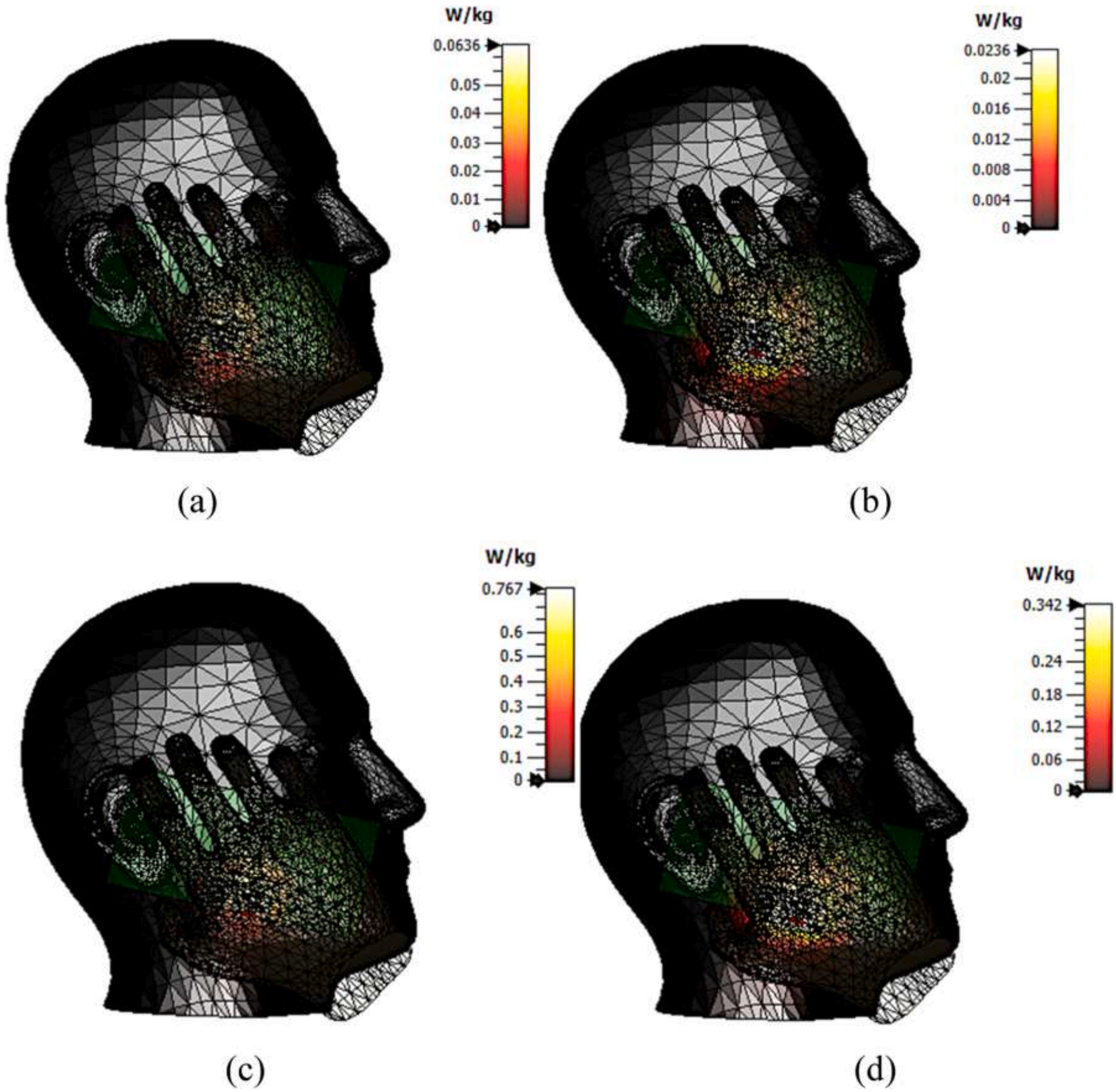

Fig. 16. SAR analysis at 15 dBm of the suggested MIMO antenna array arrangement with a rear cover at 3.3 GHz (a) 1 g and (b) 10 g and at 4.5 GHz (c) 1 g and (d) 10 g.

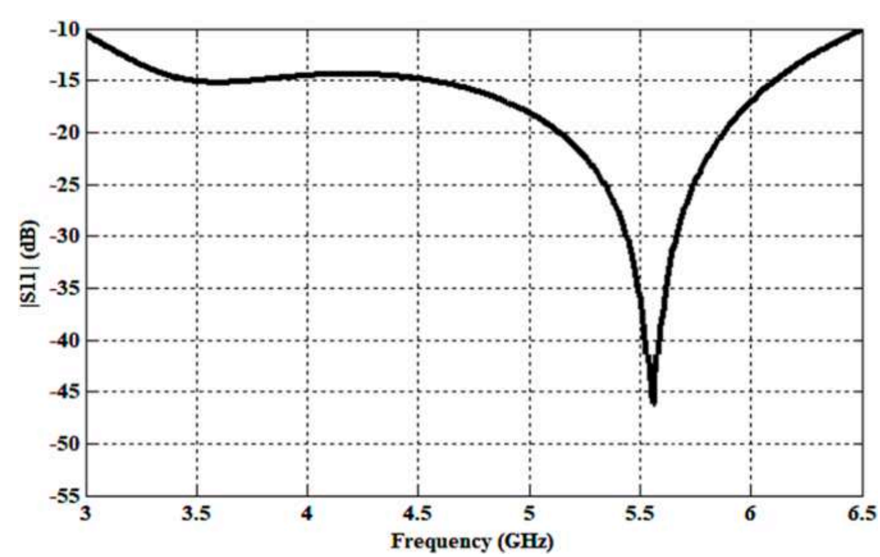

Fig. 17. S-parameter readings in data mode while the hand is present.

Table 4
Evaluation of the proposed structure's SAR1g and SAR10g at 15 dBm power.

Frequency	Distance 5 *mm*		Distance 10 *mm*	
	SAR_{1g} (W/kg)	SAR_{10g} (W/kg)	SAR_{1g} (W/kg)	SAR_{10g} (W/kg)
At 3.3 GHZ	0.0636	0.0236	0.0425	0.0145
At 4.5 GHZ	0.767	0.342	0.524	0.198

Table 5
Conducts a performance assessment by comparing the proposed methodology with previous research endeavors.

No.	Ref.	Size mm^2	Size (λ)	Ports No.	BW (GHz)	Isolation techniques	Minimum isolation (dB)	Maximum Gain (dBi)	Efficiency (%)	ECC	DG
#1	[29]	60 × 60	0.83λ × 0.83λ	4	4–5.2	EBG	− 17	8	90	< 0.2	10
#2	[30]	42 × 42	0.58λ × 0.58λ	4	5.2–5.8	H-shaped Decoupling	− 14	5	80	NA	NA
#3	[31]	40 × 30	0.55λ × 0.58λ	4	3.2–5.7	DGS	−10	3.5	82	< 0.05	9.98
#4	[32]	30 × 30	0.41λ × 0.41λ	4	4.58–6.12	L-shaped Decoupling	−15	4.02	67–82	< 0.15	9.85
#5	[33]	110 × 110	1.52λ × 1.52λ	4	5–8	Double layer metasurface	− 25	5	77	< 0.12	NA
#6	[34]	45 × 45	0.62λ × 0.62λ	2	2.2–6.28	DGS	− 14	4	91	0.025	NA
#7	[35]	45 × 59.6	0.62λ × 0.82λ	2	4.7–10.6	DGS	− 12.2	8	NA	NA	NA
#8	[36]	100 × 60	1.4λ × 0.83λ	2	1.34–3.92	EBG	− 10	5	NA	0.04	9
#9	[37]	25 × 40	0.35λ × 0.55λ	2	3.2–5.9	NL	−50	6.22	85.3	0.025	9.8
#10	[38]	60 × 40	0.83λ × 0.55λ	2	2.6–6.1	NL	−25	4.5	85	NA	NA
#11	[39]	50 × 48	0.69 λ × 0.66λ	2	2.27–2.69 5.6–5.84	NL	−35	NA	NA	< 0.3	NA
Proposed work		22 × 44	0.3 λ × 0.6λ	2	3–6.5	DGS	− 53	11.5	95	< 6 × 10^{-4}	9.9979

Where λ_0 represents the free-space wavelength.

including ECC, DG, and CCL, were derived from simulations and measurements to validate the antenna's performance. The study results consistently exhibited positive trends across the targeted frequency ranges, indicating the suitability of the proposed design for 5 G sub-6 GHz applications. Furthermore, SAR analysis confirms that the MIMO array meets safety standards for 5 G handheld mobile systems operating in this frequency range.

CRediT authorship contribution statement

Rania Hamdy Elabd: Writing – original draft, Software, Methodology, Conceptualization. **Ahmed J.A. Al-Gburi:** Writing – review & editing, Validation, Supervision, Project administration. **Amany A. Megahed:** Software, Investigation, Data curation.

Declaration of competing interest

The authors declare that they have no known competing financial interests or personal relationships that could have appeared to influence the work reported in this paper.

Acknowledgements

The authors express their gratitude to the Higher Institute of Engineering and Technology in New Damietta, Egypt, Universiti Teknikal Malaysia Melaka (UTeM), and the Ministry of Higher Education (MOHE) of Malaysia for their valuable support in facilitating this project.

Data availability

Data will be made available on request.

References

[1] A.A. Megahed, A.H. Hussein, A.J.A. Al-Gburi, R.H. Elabd, Compact wideband antenna array with DGS-based metamaterial for efficient smartphone communication and SAR reduction, Prog. Electromagn. Res. B 110 (2025) 15–28.
[2] A.J. Abdullah Al-Gburi, 5G MIMO antenna: compact design at 28/38 GHz with metamaterial and SAR analysis for mobile phones, Prz. Elektrotech. 2024 (4) (2024) 171–174.
[3] N.H.B. Jemaludin, A.J.A. Al-Gburi, R.H. Elabd, T. Saeidi, M.F. Akbar, I.M. Ibrahim, Z. Zakaria, A comprehensive review on MIMO antennas for 5 *G* smartphones: mutual coupling techniques, comparative studies, SAR analysis, and future directions, Results Eng. (2024) 102712.
[4] R.H. Elabd, A.J.A. Al-Gburi, Low mutual coupling miniaturized dual-band quad-port MIMO antenna array using decoupling structure for 5G smartphones, Discov. Appl. Sci. 6 (2024) 189, https://doi.org/10.1007/s42452-024-05765-w.
[5] A. Ali, M.E. Munir, M. Marey, H. Mostafa, Z. Zakaria, A.J.A. Al-Gburi, F.A. Bhatti, A compact MIMO multiband antenna for 5G/WLAN/WIFI-6 devices, Micromachines (Basel) 14 (2023) 1153, https://doi.org/10.3390/mi14061153.
[6] Ouafae Elalaouy, Mohammed EL Ghzaoui, Jaouad Foshi, A high-isolated wideband two-port MIMO antenna for 5G millimeter-wave applications, Results Eng. 23 (2024) 102466, https://doi.org/10.1016/j.rineng.2024.102466.
[7] Rakesh N. Tiwari, O.Sevankith Sai, Deepti Sharma, M.Shiva Kumar, Prabhakar Singh, Pradeep Kumar, Chittor Sreemanya, S. Rajasekaran, A low-profile dual-band millimeter wave patch antenna for high-speed wearable and biomedical applications, Results Eng. 24 (2024) 103212, https://doi.org/10.1016/j.rineng.2024.103212.
[8] Praveen Kumar, Ajit Kumar Singh, Ranjeet Kumar, Santosh Kumar Mahto, Pravesh Pal, Rashmi Sinha, Arvind Choubey, Ahmed Jamal Abdullah Al-Gburi, Design and analysis of low profile stepped feedline with dual circular patch MIMO antenna and stub loaded partial ground plane for wireless applications, Prog.

Electromagn. Res. C 140 (2024) 135–144, https://doi.org/10.2528/PIERC23121201.
[9] A. Sharma, H. Singh, A. Gupta, et al., Development and evaluation of wideband negative response in ultra-thin polygon metamaterial, Eur. Phys. J B97 (2024) 61, https://doi.org/10.1140/epjb/s10051-024-00692-6.
[10] S. Ghosh, G. Singh Baghel, M.V. Swati, Design of a highly-isolated, high-gain, compact 4-port MIMO antenna loaded with CSRR and DGS for millimeter wave 5G communications, AEU - Int. J. Electron. Commun. 169 (2023) 154721, https://doi.org/10.1186/s13638-023-02267-y. Sep.
[11] B.G.P. Shariff, T. Ali, P.R. Mane, M.G.N. Alsath, P. Kumar, S. Pathan, et al., Design and measurement of a compact millimeter wave highly flexible MIMO antenna loaded with metamaterial reflective surface for wearable applications, IEEE Access 12 (2024) 30066–30084.
[12] M. Farahani, J. Pourahmadazar, M. Akbari, M. Nedil, A.R. Sebak, T.A. Denidni, Mutual coupling reduction in millimeter-wave MIMO antenna array using a metamaterial polarization-rotator wall, IEEE Antennas Wirel. Propag. Lett. 16 (2017) 2324–2327.
[13] R.H. Elabd, A.J.A. Al-Gburi, Super-compact 28/38 GHz 4-port MIMO antenna using metamaterial-inspired EBG structure with SAR analysis for 5G cellular devices, J. Infrared Milli. Terahz. Waves 45 (2024) 35–65, https://doi.org/10.1007/s10762-023-00959-6.
[14] R.H. Elabd, A.J.A. Al-Gburi, Ultra-compact 4-port MIMO antenna with defected ground structure and SAR analysis for 28/38 GHz 5G mobile devices, J. Electromagn. Waves Appl. (2024) 1–26, https://doi.org/10.1080/09205071.2024.2354716. May.
[15] Z. Yang, J. Xiao, Q. Ye, Enhancing MIMO antenna isolation characteristic by manipulating the propagation of surface wave, IEEE Access 8 (2020) 115572–115581.
[16] E. Thakur, et al., Microstrip antenna with two elements and defected ground structure for 5G mobile applications at 28/38 GHz, Prog. Electromagn. Res. C 146 (2024) 177–185, https://doi.org/10.2528/PIERC24062403.
[17] R. Liu, X. An, H. Zheng, M. Wang, Z. Gao, E. Li, Neutralization line decoupling tri-band multiple-input multiple-output antenna design, IEEE Access 8 (2020) 27018–27026, https://doi.org/10.1109/ACCESS.2020.2971038.
[18] Ashish Kumar, Ashwini Kumar, Ahmed Jamal Abdullah Al-Gburi, Development of semi-circular corner cut MIMO antenna for 5G-advanced and 6G automotive wireless applications, Results Eng. 25 (2025) 103805, https://doi.org/10.1016/j.rineng.2024.103805.
[19] Y.-F. Cheng, J. Liu, C. Wei, W.-J. Wu, L. Sun, G. Wang, Interplanted patch-monopole array with enhanced isolation, IEEE Antennas Wirel. Propag. Lett. 21 (2022) 1664–1668.
[20] X. Zhao, S.P. Yeo, L.C. Ong, Planar UWB MIMO antenna with pattern diversity and isolation improvement for mobile platform based on the theory of characteristic modes, IEEE Trans. Antennas Propag. 66 (2018) 420–425.
[21] A. Sharma, K.P. Kalaskar, J.R. Gangane, Analysis of MIMO antennas with parasitic elements for wireless applications, in: Proceedings of the 2016 IEEE International Conference on Computational Intelligence and Computing Research (ICCIC), Chennai, India, 2016, pp. 1–4, 15–17 December.
[22] R.H. Elabd, A.J.A. Al-Gburi, SAR assessment of miniaturized wideband MIMO antenna structure for millimeter wave 5G smartphones, Microelectron. Eng. 282 (2023), https://doi.org/10.1016/j.mee.2023.112098.
[23] D. Zhang, Y. Chen, S. Yang, A self-decoupling method for antenna arrays using high-order characteristic modes, IEEE Trans. Antennas Propag. 70 (2022) 2760–2769.
[24] W. Yang, L. Chen, S. Pan, W. Che, Q. Xue, Novel decoupling method based on coupling energy cancellation and its application in 5G dual-polarized high-isolation antenna array, IEEE Trans. Antennas Propag. 70 (2022) 2686–2697.
[25] E. Thakur, N. Jaglan, A. Gupta, A.J.A. Al-Gburi, Multi-band notched circular polarized MIMO antenna for ultra- wideband applications, Prog. Electromagn. Res. M 125 (2024) 87–95.
[26] Preeti Sharma, Rakesh Nath Tiwari, Prabhakar Singh, Circumferential slots based decoupled wideband MIMO antenna for 5G and sub-6 GHz applications, Phys. Scr. 99 (6) (2024) 065012, https://doi.org/10.1088/1402-4896/ad43c9.
[27] M.M. Basha, P. Pradeep, S. Gundala, J. Syed, Design of compact and high gain dual-band four-port MIMO antenna array for mm-wave 5G communications, Results Eng. 25 (2025) 104153, https://doi.org/10.1016/j.rineng.2025.104153. Mar.
[28] W.A. Ali, A.A. Ibrahim, A.E. Ahmed, Dual-band millimeter wave 2 x 2 MIMO slot antenna with low mutual coupling for 5G networks, Wirel. Pers. Commun. 129 (2023) 2959–2976.
[29] W. Wu, B. Yuan, A. Wu, A quad-element UWB-MIMO antenna with band-notch and reduced mutual coupling based on EBG structures, Int. J. Antennas Propag. 2018 (2018). Feb.Art. no. 8490740.
[30] Y. Luo, Q.-X. Chu, J.-F. Li, Y.-T. Wu, A planar H-shaped directive antenna and its application in compact MIMO antenna, IEEE Trans. Antennas Propag. 61 (9) (2013) 4810–4814. Sep.
[31] J. Kulkarni, A. Desai, C.-Y.-D. Sim, Wideband four-port MIMO antenna array with high isolation for future wireless systems, AEU- Int. J. Electron. Commun. 128 (2021), https://doi.org/10.1016/j.aeue.2020.153507. Jan.Art. no. 153507.
[32] M. Yang, J. Zhou, A compact pattern diversity MIMO antenna with enhanced bandwidth and high-isolation characteristics for WLAN/5G/WiFi applications, Microw. Opt. Technol. Lett. 62 (6) (2020) 2353–2364.
[33] J. Tang, F. Faraz, X. Chen, Q. Zhang, Q. Li, Y. Li, S. Zhang, A metasurface superstrate for mutual coupling reduction of large antenna arrays, IEEE Access 8 (2020) 126859–126867.
[34] R. Anitha, P.V. Vinesh, K.C. Prakash, P. Mohanan, K. Vasudevan, A compact quad element slotted ground wideband antenna for MIMO applications, IEEE Trans. Antennas Propag. 64 (10) (2016) 4550–4553.
[35] X.-J. Zou, G.-M. Wang, Y.-W. Wang, B.-F. Zong, Mutual coupling reduction of Quasi-Yagi antenna array with hybrid wideband decoupling structure, AEU-Int. J. Electron. Commun. 129 (2021). Feb.Art. no. 153553.
[36] S. Roy, U. Chakraborty, Mutual coupling reduction in a multi-band MIMO antenna using meta-inspired decoupling network, Wirel. Pers. Commun. 114 (4) (2020) 3231–3246. Oct.
[37] K. Vasu Babu, Sudipta Das, Syed Samser Ali, Shobhitkumar Kiritkumar Patel, Broadband sub-6 GHz flower-shaped MIMO antenna with high isolation using theory of characteristic mode analysis (TCMA) for 5G NR bands and WLAN applications, Int. J. Commun. Syst. 36 (6) (2023).
[38] K. Vasu Babu, B. Anuradh, Design of Wang shape neutralization line antenna to reducethe mutual coupling in MIMO antennas, Analog Integr. Circuits Signal Process. 101 (2019) 67–76.
[39] Yitian Sun, Minmin Tian, G.S. Cheng, Characteristic mode-based neutralization line design for MIMO Antenna, Int. J. Antennas Propag. 2022 (2022), https://doi.org/10.1155/2022/9669114.